



# Solar-cycle, seasonal, and asymmetric dependencies of thermospheric mass density disturbances due to magnetospheric forcing

Andres Calabia<sup>1</sup>, and Shuanggen Jin<sup>1</sup>

<sup>1</sup>School of Remote Sensing and Geomatics Engineering, Nanjing University of Information Science and Technology, Nanjing 210044, China

Correspondence to: SG Jin (sgjin@nuist.edu.cn)

**Abstract.** Short-term upper atmosphere variations due to magnetospheric forcing are very complex, and neither well understood nor capably modelled due to limited observations. In this paper, mass density variations from 2003-2013 of GRACE observations are isolated through the parameterization of annual, Local-Solar-Time (LST), and solar-cycle fluctuations using a Principal Component Analysis (PCA) technique and investigated in terms of magnetospheric drivers. The magnitude of high-frequency (< 10 days) disturbances shows unexpected dependencies on solar-cycle, seasonal, and an asymmetric behaviour based on weaker variations in June at the South Polar Region (SPR). We suspect this seasonal modulation might be related to the Russell-McPherron (R-M) effect, and find a similar pattern, but less pronounced at the northern and equatorial regions. A possible cause of this latitudinal asymmetry might be the irregular shape of Earth's magnetic field (with the north dip pole close to Earth's rotation axis, and the south dip pole far from that axis). After accounting for solar-cycle and seasonal dependencies by regression analysis to the magnitude of the high-frequency perturbations, the parameterization in terms of  $Dst$  shows good correlation, while  $A_m$  and  $E_m$  are best predictors. We test several mass density models, including JB2008, NRLMSISE-00, and TIEGCM, and find that they are unable to completely reproduce the seasonal and solar-cycle trends found in this study, and with a clear overestimation of about 100% during low solar activity periods.

## 1 Introduction

### 1.1 Solar driving and MIT system phenomena

The connection between solar drivers and Magnetosphere-Ionosphere-Thermosphere (MIT) phenomena is very complex and dependent on many processes. One of the most important processes is the variable solar wind plasma combined with a favourable alignment of the IMF, which can produce auroral particle precipitation at high-latitudes and increment of thermospheric Joule heating through coupled MIT processes linked to the Dungey cycle [Dungey, 1961]. This phenomena can suddenly govern the structure and dynamics of the thermosphere, creating changes in mass density distribution through thermal expansion/contraction and changes in composition of neutral species (i.e.,  $O/N_2$  depletion [Lei *et al.* 2010]). For



30 instance, solar flares increase the X-ray and Extreme Ultra-Violet (EUV) irradiance, and produce nearly immediate energy-  
absorption, ionization, and dissociation of molecules. Occurrence of solar flares usually correlate to the rotational variation  
of the Sun (about 27 day and sub-harmonics at about 9 day, 7 day, and 5 day), resulting from the secular appearances of  
bright regions associated with sunspots that persist across solar rotations. Different sunspots regions in the solar corona  
provide different speeds and densities of solar wind, forming an outward spiral with fast-moving and slow-moving streams.  
35 Fast moving solar wind tends to overtake slower streams, forming turbulent Co-rotating Interaction Regions (CIR). In  
addition, Coronal Mass Ejections (CME) release fast-moving bursts of plasma at the corona of the Sun, which travels at  
higher speeds than CIRs. CIR and CME's create magnetospheric storms, which are mainly driven by the electric fields  
linked to the Dungey cycle. CMEs can produce stronger storms than CIRs, and are usually initiated by a southward IMF,  
enhancing the night-side convection, and increasing the ring current. When CIRs and CMEs reach Earth, the rapid increase  
40 in Poynting flux and particle precipitation along the Earth's magnetic field lines, originating from solar-wind/magnetosphere  
coupling processes, lead to an enhancement in Joule heating and disturbances in thermospheric composition, temperature,  
density, and winds. First effects of CMEs and CIRs appear in the auroral zone as an increase in thermospheric mass density,  
and shortly afterwards the perturbation propagates equator-ward, followed by a global expansion lasting from several hours  
up to several days.

#### 45 **1.2. Existing thermospheric modeling**

Thermospheric mass density distribution particularly during storm-time is of great importance for Low Earth Orbit (LEO)  
Precise Orbit Determination (POD), and for the understanding of MIT coupling. However, the energy transfer from the solar  
wind to the MIT system is complex, not completely described by models and observations, and many studies focus their  
efforts on a better understanding of all involved physical processes. Currently, atmospheric drag from mass density at LEO is  
50 the largest uncertainty in orbit determination and prediction, because short-term variations produced by episodic solar  
activity, for example, are still not well modelled (e.g., *Marcos et al.* [2010]). Currently, Mass Spectrometer and Incoherent  
Scatter radar (NRLMSISE00) [*Picone et al.*, 2002], *Jacchia* [*Bowman et al.*, 2008], and Thermosphere-Ionosphere-  
Electrodynamics General Circulation Model (TIEGCM) [*Qian et al.*, 2014] are the most representative models of mass-  
density variations in the upper atmosphere. While the mathematical formulation of NRLMSISE00 uses the exponential Bates  
55 profile [*Bates*, 1959], the *Jacchia* series use the arctangent function to represent an asymptotic behaviour for the upper  
thermosphere. On the other hand, the first-principles TIEGCM physical model solves three-dimensional fluid equations for  
the mutual diffusion of  $N_2$ ,  $O_2$ , and  $O$ , including a coupled ionosphere, where the reactions involve ion species and energy  
budget, as well as self-consistent generation of middle and low latitude electric fields by neutral winds.

#### **1.3. Thermospheric mass density responses to geomagnetic storms**

60 During the last decade, considerable progresses have been achieved on observing and modeling responses to geomagnetic  
storms in the thermosphere. For instance, *Liu et al.* [2005] firstly showed from mass density estimates retrieved from



Challenging Minisatellite Payload (CHAMP) accelerometer measurements two structured arc-shaped enhancements of  $\sim$  2000 km diameter in the auroral regions. *Liu and Lühr* [2005] and *Sutton et al.* [2005] investigated the severe geomagnetic storm of November 2003 from CHAMP and, shortly afterwards, *Bruinsma et al.* [2006] included the Gravity Recovery and  
65 Climate Experiment (GRACE) estimates to investigate the same storm, showing density increases up to 800 %. *Rentz and Lüh,* [2008] studied the climatology of the cusp-related thermospheric mass density anomalies as derived from CHAMP over 4 years (2002-2005), and showed an increase in density anomaly proportional to the square of the merging electric field  $E_m$ . *Sutton et al.* [2009] studied the response to variations produced by the July 2004 geomagnetic storm from CHAMP, showing a time response significantly shorter than those used by the empirical models. Based on the variations of the ratio of density  
70 estimates between ascending and descending orbits, *Muller et al.* [2009] showed a slightly better parameterization of mass density employing the  $Am$  index instead the  $Ap$  index. *Lathuillère, et al.* [2008] also showed a better correlation with the magnetic  $Am$  index than with the  $Ap$  index from one year of CHAMP-derived densities, and revealed a similar behavior between the day and the night side variations. Moreover, *Guo et al.* [2010] and *Liu et al.* [2010, 2011] investigated a large number of great storms ( $Dst \leq -100$  nT) and showed similar correlations on the day-side to those on the night-side.

75 Concerning seasonal and inter-hemispheric asymmetries, several studies have identified and investigated the possible dependence on magnetospheric forcing. For instance, *Lu et al.* [1994] found a significant difference in the cross-polar-cap potential drop between the two hemispheres (when  $B_z$  is positive and  $|B_y| > B_z$ ), with a potential drop in the southern (summer) hemisphere over 50% larger than that in the northern (winter) hemisphere. *Fuller-Rowell et al.* [1996] explained that a latitudinal asymmetry of the global thermospheric mass density distribution would be explained in terms of the  
80 prevailing summer to winter meridional flow, and *Forbes et al.* [1996] included to this explanation the different solar-driven meridional contributions at the day and night sides. *Fuller-Rowell* [1998] proposed a new mechanism based on huge turbulent eddy mixing due to the seasonal inter-hemisphere thermospheric circulation, partially mixing the thermospheric species, and restricting their diffusive separation. The authors suggested that during solstice periods, this "thermospheric spoon mechanism" could be triggered by strong inter-hemispheric prevailing meridional winds originated by a global  
85 pressure gradient due to the asymmetric heating of the globe. The resulting inter-hemispheric asymmetry distribution of mass density could not be created during equinox periods, because of the resulting weak latitude pressure gradients and light meridional winds from equilibrium between the high-latitude and low-latitude sources of heating. More recently, *Bruinsma et al.* [2006] also showed a latitudinal asymmetry with higher mass density values at the southern latitudes, and suggested an enhanced summer versus winter Joule heating at high latitudes. *Ercha et al.* [2012] studied the hemispheric asymmetry of the  
90 thermospheric response to geomagnetic storms through a statistical analysis of 102 geomagnetic storms (2001 - 2007), showing much larger density enhancements in the South Polar Region (SPR) than in the North Polar Region (NPR). The authors attributed these phenomena to the non-symmetric Earth's magnetic field. Moreover, *Deng et al.* [2014] examined the high latitude asymmetry in the Pedersen conductance from electron density profiles during 2008 to 2011, showing larger



changes of energy partition between the ionospheric E (100-150 km) and F (150-600 km) regions in the southern hemisphere  
95 than in the northern hemisphere.

#### 1.4. Preamble

The above review describes the big picture of the current efforts done for a better understanding of mass density variations driven by magnetospheric forcing, and its modelling through correlations to their representative proxies. However, the sufficiently accurate set of drivers, proxies, and interrelations between involved geophysical processes is still incomplete,  
100 and more studies for a better understanding and modelling are needed. For instance, a proper removal of annual, LST, and solar cycle variation is key to unambiguously resolve the relation between proxies of magnetospheric forcing and mass density disturbances, and none of previous authors have investigated a sufficiently large and continuous time-series of observations, at least to complete a solar cycle, while their statistical analysis were focused only on collections of large storms. In this manuscript, we present a comprehensive study on thermospheric density disturbances due to magnetospheric  
105 forcing from 10-year (2003-2013) continuous time-series of GRACE accelerometer and POD -based mass density estimates, which have been isolated from annual, LST, and solar cycle variations through the parameterization of the Principal Component Analysis (PCA) [Calabia and Jin, 2016]. In this scheme, a continuous time-series can provide a more realistic representation during both active and quiet magnetospheric conditions, instead analyzing a collection of large storms. The structure of this manuscript is presented as follows: Section 2 describes the data sets and analysis methods employed;  
110 Section 3 presents the results on dependencies and asymmetries from correlations and parameterizations at high and low latitudes; comparison with the current models as well as discussion are given in Section 4; and finally summary and conclusions are given in Section 5.

## 2. Data and analysis methods

### 2.1. Mass density estimates and geomagnetic indices

115 We employ thermospheric mass densities inferred from accelerometer and POD measurements made by the GRACE mission [Tapley *et al.*, 2004]. The GRACE satellites were launched into a near-circular orbit on 17 March 2002 with an initial altitude of about 525 km, and a mean altitude of 475 km. The highly sensitive accelerometers on-board the GRACE satellites were originally designed to measure the Earth's gravity field, but the measurements of non-gravitational forces have provided the unprecedented opportunity to derive and study thermospheric mass density variations. In this study, mass  
120 density estimates are computed using the methods developed in Calabia and Jin [2016], and are provided at 3 min interval sampling in the supporting information files. The detailed processing steps can be found in the same reference and in Calabia and Jin [2017] and Calabia [2017]. Space weather and geomagnetic indices have been downloaded in the Low Resolution OMNI (LRO) data set of NASA (<http://omniweb.gsfc.nasa.gov/form/dx1.html>), and from the International Service of Geomagnetic Indices (ISGI) website ([http://isgi.unistra.fr/data\\_download.php](http://isgi.unistra.fr/data_download.php)). The merging electric field,  $E_m$ ,



125 assumes that there is an equal magnitude of the electric field in the solar wind, the magnetosheath, and on the magnetospheric sides of the magnetopause [Kan and Lee, 1979]:

$$E_m = v_{SW} \sqrt{B_y^2 + B_z^2} \sin^2 \left( \frac{\theta}{2} \right) \quad (1)$$

where  $B_y$  and  $B_z$  are the IMF components,  $v_{SW}$  is the solar wind speed, and  $\theta$  the IMF clock angle in Geocentric Solar Magnetospheric (GSM) coordinates.

### 130 2.2. Parameterization of solar cycle, annual, and LST variations

In order to remove solar cycle, annual, and LST variations from the original density estimates, we employ the parameterization of the main modes provided by the PCA of 13 years of GRACE data provided in Calabia and Jin [2016]. We have included the model in the supporting information files. The aim of by 'a' PCA technique is to determine a new set of bases that capture the largest variance in the data based on Eigen Value Decomposition of the sample covariance estimated from the original data. In this study, the four leading modes together account for 99.8 % of the total variance and, individually, explain 92 %, 3.5 %, 3 %, and 1.3 % of the total variability. The correlation coefficients between the parameterized time series of PCA modes and the originals are 96 %, 93 %, 90 %, and 83 %, respectively. The highly values of explained variance for the first modes indicate marked patterns of variability, and the correlations to parameterizations indicate high accuracy in the model. In order to reflect the magnetospheric contribution through relevant proxies in the residuals, we employ a constant value of  $Am=6$  in the parameterization given by Calabia and Jin [2016]. Herein refer the parameterization set of solar cycle, annual, and LST variations as "radiation model" ( $\rho_{model}$ ), while the residuals ( $\rho_r$ ) to mass density estimates ( $\rho_{GRACE}$ ) are defined as:

$$\rho_r = \rho_{GRACE} - \rho_{model} \quad (2)$$

Assuming high efficiency in the model ( $\rho_{model}$ ), the residual disturbances ( $\rho_r$ ) will not only contain variations due to magnetospheric forcing, but also disturbances due to other sources, as for example, lower atmospheric waves and recurrent Travelling Atmospheric Disturbances (TADs) [Bruinsma and Forbes, 2010]. These other disturbances are not regarded in this manuscript, and can be investigated in future research after removal of the presented model. More complete listing of known thermospheric mass density disturbances is given in Liu et al., [2017].

### 2.3. Density responses to magnetospheric forcing at different latitudes

150 Density residuals at three latitude regions are extracted from the residual disturbances to form North, Equator, and South profiles to determine their time-dependent relationship to changes in magnetospheric drivers. We denote  $\rho_r$  in Eq. 2 as  $\rho_E$  for the profile at Equator, and  $\rho_N$  and  $\rho_S$  for the NPR and SPR profiles, respectively. Density profiles for each region (see



example in Fig. 1a) correspond to an average value of density of a longitudinal band of 30° width in latitude, centered at Equator ( $\rho_E$ ) and at the geographic poles ( $\rho_N$ ,  $\rho_S$ ). The Equator profile of density is computed as the mean average between ascending and descending orbits, so possible LST and time-lag differences between ascending and descending orbits are mitigated (some studies introduced in Section 1.3.3. have shown a negligible contribution).

The approach employed in this work is based on the parameterization of the standard deviation, which provides a more robust metric modeling, instead of attempting to fit the direct signal of disturbances. Additional smoothing filters are applied to both residual disturbances and proxies as follows. First, we remove the disturbances longer than 10 day period from both  $\rho_r$  and geomagnetic indices to further standardize the data sets. We divide the approach in two steps, one for sub-daily variations, and the other for those between 1 and 10 days. The removal of longer trends is performed by subtracting the smoothed time-series with a 10-day running-window filter, and the sub-daily variations are extracted in a similar way through a 1-day running-window filter. The general form for the mean running-window filter is:

$$F(x)_i = \sum_{j=i-a}^{i+a} \frac{x_j}{(2a+1)} \quad (3)$$

Where  $x_i$  is the time-series to filter at each index  $i$ ,  $a$  is half of the increment of time for each corresponding running-window, and  $F(x)$  is the smoothed time-series employed to remove long-term signals.

The standard deviation shown in Fig. 2 is calculated for each pair of time-series ( $\rho_r < 1$  day, and  $1 \text{ day} < \rho_r < 10$  day) through a 30-day running window (we employ a similar form of Eq. 3 to compute the standard deviation instead of the mean value). Fig. 2 reveal strong dependencies on solar cycle, we further parameterize this dependence in terms of solar-flux F10.7 (Fig. 3, Table 1), and the results are given in Fig. 4. A seasonal dependency is shown with weaker disturbances during June solstice periods, mostly at the SPR. We parameterize this seasonal variation to better fit geomagnetic indices into the residual disturbances ( $\rho_r$ ), by using the annual period in a Fourier fitting to the normalized disturbance in the SPR (Table 2). After this seasonal variation is removed, the normalized standard deviations of the residual disturbances ( $\rho_r$ ) show good agreement with the standard deviations of the geomagnetic indices. The fitting of least absolute residuals (which minimizes the absolute difference of the residuals) in a 2-variable parameterization (solar-cycle and geomagnetic index) is chosen to better characterize singular events of strong geomagnetic activity:

$$\begin{aligned} \rho_r' = & p_{00} + p_{10} \cdot \text{Ind} + p_{01} \cdot F + p_{20} \cdot \text{Ind}^2 + p_{11} \cdot \text{Ind} \cdot F + p_{02} \cdot F^2 + \\ & + p_{30} \cdot \text{Ind}^3 + p_{21} \cdot \text{Ind}^2 \cdot F + p_{12} \cdot \text{Ind} \cdot F^2 \end{aligned} \quad (4)$$



180 Where  $Ind$  correspond to the geomagnetic index employed ( $A_m$ ,  $Dst$ , and  $E_m$ ), and  $F$  is the solar radio flux at 10.7 cm. As for the SPR, we easily modulate the parameterized northern profile in terms of the parameterized disturbances at the SPR,  $\sigma''$  (Table 2):

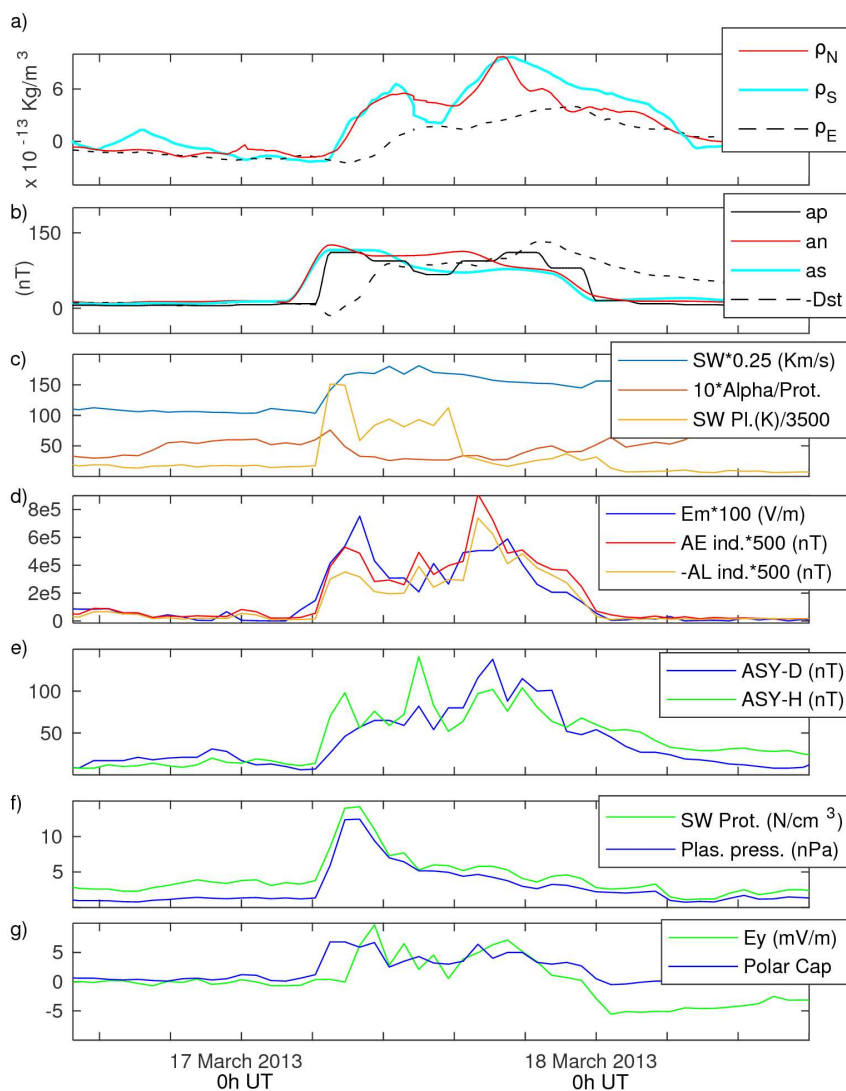
$$\begin{aligned} \rho_S' = & p_{00} + p_{10} \cdot \rho_N' + p_{01} \cdot \sigma'' + p_{20} \cdot \rho_N'^2 + p_{11} \cdot \rho_N' \cdot \sigma'' + \\ & + p_{02} \cdot \sigma''^2 + p_{30} \cdot \rho_N'^3 + p_{21} \cdot \rho_N'^2 \cdot \sigma'' + p_{12} \cdot \rho_N' \cdot \sigma''^2 \end{aligned} \quad (5)$$

185 Finally, Pearson's linear correlation coefficients between each profile of density disturbances and the final parameterizations are calculated with delay-times ranging from  $\pm 18$  h. Analysis results are provided in next section.

### 3. Results and analysis

Fig. 1a shows the northern ( $\rho_N$ ), southern ( $\rho_S$ ), and equatorial ( $\rho_E$ ) profiles of mass density disturbances, normalized to 475 km altitude for the Moderate Geomagnetic Storm (rated as G2 in the NOAA's geomagnetic storm scale) of March, 18<sup>th</sup>,  
 190 2013. Shown are traces of mass density estimates with solar cycle, annual, and LST dependencies removed. The following panels display the K-derived planetary indices ( $ap$ ,  $an$ ,  $as$ ), the auroral index horizontal component disturbances ( $AE$ ,  $AL$ ), the solar wind ( $SW$ ) velocity, proton and temperature, the longitudinally asymmetric horizontal component disturbances ( $ASY-D$ ,  $ASY-H$ ), the Electric Field ( $E_y$ ), and the Polar Cap index horizontal component disturbances.

In general, density perturbations and space weather and geomagnetic indices remain calm until early morning ( $\sim 5$  h UT) on  
 195 17<sup>th</sup> March 2013, and the geomagnetic storm commences. High latitude mass density profiles exhibits two peaks, a relative maximum at 10 h UT with  $6 \cdot 10^{-13}$  kg/m<sup>3</sup>, and an absolute maximum the same day at 17 h UT with  $9 \cdot 10^{-13}$  kg/m<sup>3</sup>. The equatorial variation shows a delay, starting the relative maximum at  $\sim 7$  h UT, and reaching the absolute maximum of  $4 \cdot 10^{-13}$  kg/m<sup>3</sup> at 22 h UT. The maximum of the equatorial density disturbance is less obvious but peaks at 10 h UT. In this figure, the  $Dst$  index shows best match with equatorial mass density disturbances. On the other hand, best match for high latitude  
 200 density disturbances is given with K-derived planetary indices ( $ap$ ,  $an$ ,  $as$ ),  $E_m$ , and the auroral index horizontal component disturbances ( $AE$ ,  $AL$ ). This is expected based on locations of magnetometer stations that contribute to the corresponding indices. Finally, all indices start to return to the calm state at the end of the day ( $\sim 24$  h UT), while the mass density profiles remain elevated until next day at  $\sim 7$  h UT (18<sup>th</sup> March 2013). This phenomenon is the atmospheric response to equilibrate the global mass density back to the initial calm state. The question that arises from this figure is whether this is a typical  
 205 storm-time behaviour, and the extent to which this behaviour could be modelled using their representative proxies in terms of time-delay, and other possible dependencies as, for example, an increasing in solar flux, or due to latitudinal asymmetries seen in previous studies (e.g., Ercha et al. [2012]; Bruinsma et al. [2006]; Fuller-Rowell et al. [1996]; Forbes et al. [1996]).

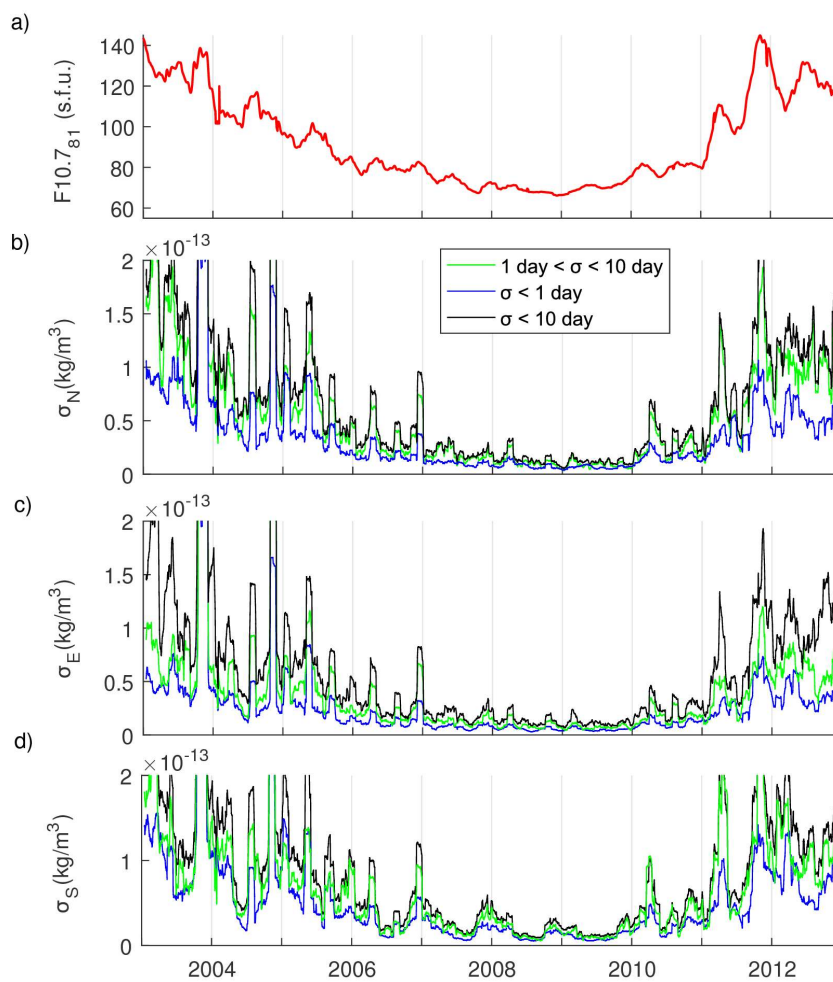


210 **Figure 1.** In (a), the northern, southern, and equatorial profiles of residual density disturbances ( $\rho_r$ ) are shown for the Moderate (G2) Geomagnetic Storm of March 18<sup>th</sup>, 2013 (free from solar cycle, LST, and annual variations, and normalized to 475 km altitude). Space weather and geomagnetic indices are plotted below from (b) to (g). Magnitudes have been re-scaled as indicated in each legend.

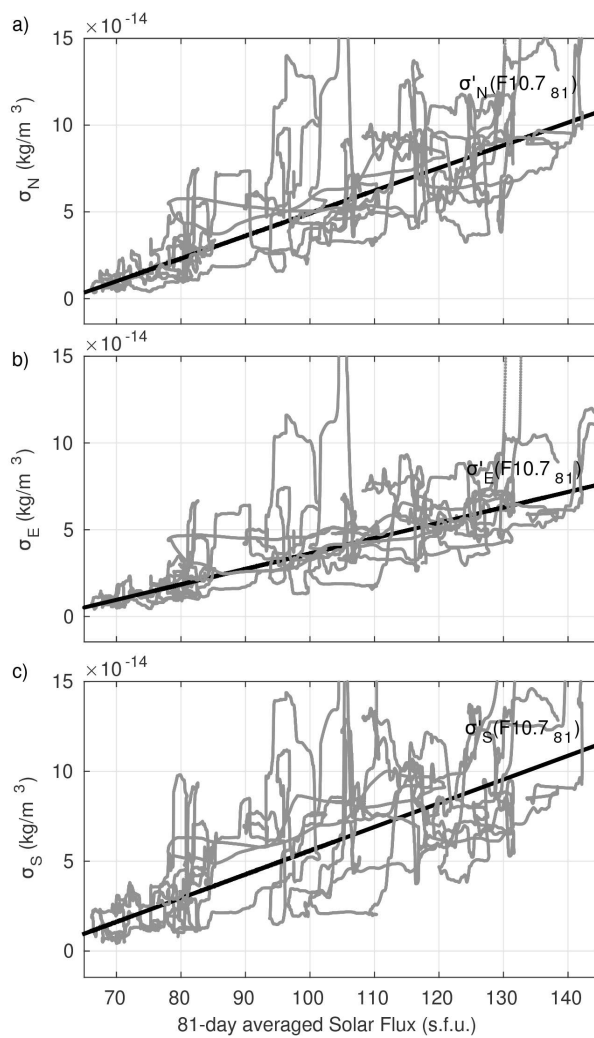
In Fig. 2, the standard deviation calculated over a sliding window of 30-day length ( $\sigma$ ) is shown for the NPR, Equator, and SPR ( $\sigma_N$ ,  $\sigma_E$ , and  $\sigma_S$ ) over the entire span of 10-year analysis period. Possible unwanted variation with long-term periods, 215 resulting from the process of removing solar cycle, annual, and LST variations has been eliminated by running a 10-day



smoothing filter. In order to detect a possible variation of the geographical influence induced by the spatial component of the PCA model (e.g., location of magnetic dip, irregular magnetic field), standard deviations have been separately computed for the initial residual disturbances, and from both sub-daily and 1-10 day disturbances. As expected, sub-daily disturbances are smaller in magnitude when comparing to the longer periods. Concerning the latitudinal differences, disturbances at the southern region ( $\rho_S$ ) are bigger in amplitude ( $\sigma_S$ ) compared to the northern region ( $\sigma_N$ ). The values are described by the fitting in Fig. 3 and Tab. 1. At first look, the residual disturbances show strong alignment with the solar-cycle trend ( $F10.7_{81}$ ), indicating that the magnitude of mass density disturbances due to magnetospheric forcing are strongly dependent on the 11-year solar cycle. Fig. 2 includes the 81-day averaged F10.7 solar-flux index to show the alignments. Note that these dependences are intrinsic to the magnitude of disturbances due to magnetospheric forcing and not from the background LST, seasonal, and solar-cycle variations which have been removed by the PCA model and smoothing procedures. In this scheme, the  $F10.7_{81}$  index is firstly employed to fit the magnitude of disturbances, and the linear fits are presented in Fig. 3 and Tab. 1.



230 **Figure 2.** From top to bottom, (a) the 81-day averaged F10.7 solar flux index, and the 30-day standard deviation sliding window of residual density disturbances at 475 km altitude in (b) the northern, (c) the equatorial, and (d) the southern regions. Calculations filtered at different frequencies are plotted in red, blue, and black.



235 Figure 3. Linear fit of 30-day standard deviation sliding window of residual density disturbances at 475 km altitude from Fig. 2 at (a) NPR and (b) SPR with respect to 81-day averaged F10.7 solar flux index. Note that annual variations haven't been removed from (c).



**Table 1. Parameters and goodness of linear fit in Fig. 3.  $\sigma'(F10.7_{81}) = p1 \cdot F10.7_{81} + p2$ .**

|                           | $\sigma'_N$              | $\sigma'_E$              | $\sigma'_S$              |
|---------------------------|--------------------------|--------------------------|--------------------------|
| p1                        | 1.3060E-15               | 8.8830E-16               | 1.3200E-15               |
| 95% conf.                 | (1.304e-15, 1.308e-15)   | (8.871e-16, 8.895e-16)   | (1.318e-15, 1.323e-15)   |
| p2                        | -8.1430E-14              | -5.2570E-14              | -7.6190E-14              |
| 95% conf.                 | (-8.161e-14, -8.125e-14) | (-5.269e-14, -5.246e-14) | (-7.645e-14, -7.593e-14) |
| R-square                  | 0.93                     | 0.96                     | 0.89                     |
| RMSE (kg/m <sup>3</sup> ) | 1.39E-14                 | 8.99E-15                 | 2.03E-14                 |

240 An interesting feature in the resulting fit of Fig. 4 is the decrease of standard deviation in southern profile ( $\sigma_S$ ) during June, clearly present in both sub-daily and 1-10 day time-series. On the other hand, the northern region  $\sigma_N$  is more aligned with the F10.7<sub>81</sub> solar cycle variation, and without strong signs of a seasonal fluctuation (refer to next section for more details). The discussion of the possible effects of this seasonal and asymmetric variation is given in the next section. The top panel in Fig. 4 plots the standard deviation computed with a 30-day sliding window of the *Am* and *Dst* geomagnetic indices, as well as the

245 *E<sub>m</sub>*. After accounting for solar-cycle variation effects by data normalization using the parameters given in Tab. 1, the standard deviation computed using the same 30-day sliding window (three bottom panels in Fig. 4) show a much better correspondence with the fitting of *Am*, *Dst*, and *E<sub>m</sub>* standard deviations ( $\sigma'$ ). Though, in the southern region (bottom panel in Fig. 4), lower mass density disturbances during summer seasons is now more obvious, and it has been parameterized in terms of day of the year (*day*). The corresponding parameters and goodness of the Furrier fit are given in Tab. 2. We employ

250 this parameterization to better characterize the fitting scheme of proxy candidates and additional dependencies. From Fig. 3 and 4, a clear contribution of solar-cycle for high and low latitudes is requisite for the fitting scheme (Eq. 4). In addition, the identified seasonal variation prominently modulates the fluctuations in the SPR. The last parameter to account for is the lag-time between proxies and density disturbances. Pearson's linear correlation coefficients between each profile of density and the final parameterizations are calculated with delay-times ranging from  $\pm 18$  h. Then, the maximum values for each time-

255 series are employed in the fitting.

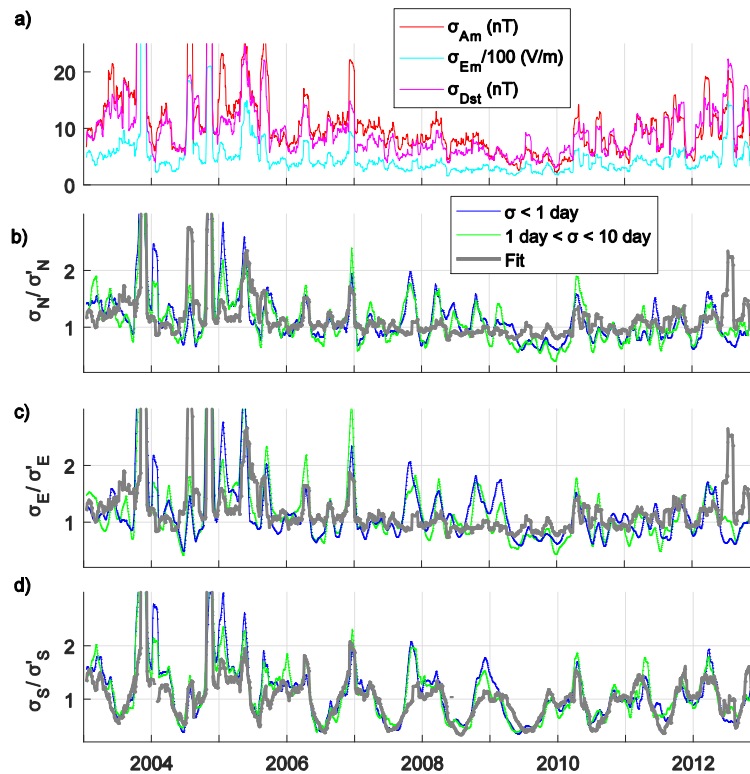


Figure 4. From top to bottom, (a) the 30-day moving standard deviation of  $A_m$ ,  $Dst$ , and  $E_m$ , and the solar-flux normalized 30-day standard deviation sliding window of residual density disturbances at 475 km altitude at (b) the northern, (c) equatorial, and (d) southern regions. Fourier fits in terms of  $doy$  and  $E_m$  are plotted in gray colour. Calculations filtered at different frequencies are plotted in green, and blue.

260



**Table 2. Parameters and goodness of Furrrier fit (Fig. 4).  $\sigma''(doy) = 1 + a1 \cdot \cos(doy) + b1 \cdot \sin(doy) + a2 \cdot \cos(2 \cdot doy) + b2 \cdot \sin(2 \cdot doy)$**

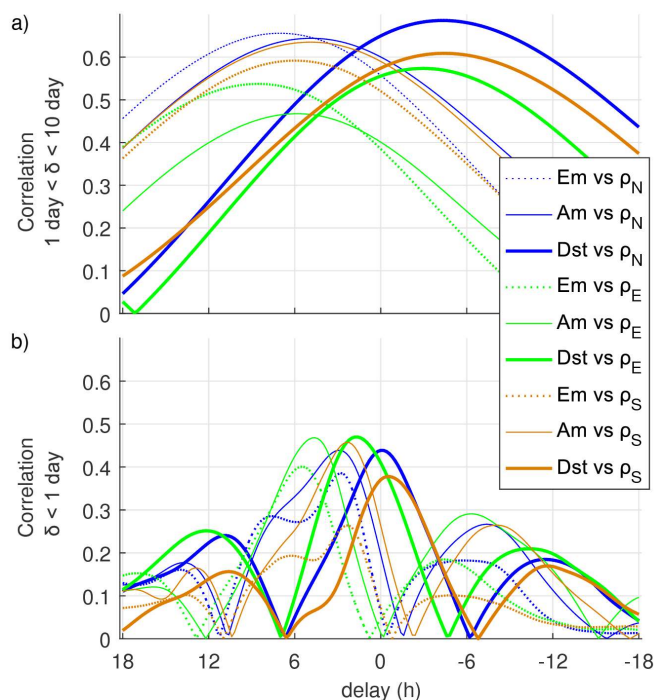
|                           | $\sigma''_N$ | $\sigma''_S$                  |
|---------------------------|--------------|-------------------------------|
| a1                        | -            | 0.3893 (0.3876, 0.3909)       |
| b1                        | -            | 0.1043 (0.1027, 0.1059)       |
| a2                        | -            | -0.1448 (-0.1464, -0.1431)    |
| b2                        | -            | -0.05656 (-0.05817, -0.05494) |
| R-square                  | -            | 0.80                          |
| RMSE (kg/m <sup>3</sup> ) | -            | 2.62E-01                      |

265 Fig. 5 plots the lag-time correlation coefficients between the parameterized perturbations and the three northern, equatorial, and southern profiles of residual disturbances ( $\rho_r$ ). The top panel in Fig. 5 corresponds to density disturbances on frequencies ranging from 1 to 10 days and the bottom panel corresponds to sub-daily disturbances. In general, sub-daily disturbances exhibit a smaller range of time-lag for correlations with drivers, than the longer variations shown in the top panel. A secondary maximum at about 12 h ahead of the absolute maximum might probably be originated by TADs reaching the opposite side of the globe, but further study is required to validate this assumption. Negative values proceeding to geomagnetic storms could also increase the secondary maximum. Negative values at equator prior to geomagnetic storms have been reported in earlier studies [Calabia and Jin, 2017], and further discussion in relation to the *Dst* index is given in the next section. Both time-delays of 1 to 10 days and sub-daily correlations show similar response to the *Dst* index, showing a delay occurring after density disturbances, and revealing a shortcoming for prediction. On the other hand,  $A_m$  and  $E_m$  have much more capability as predictors. For the high latitude profiles, lag-time correlation of  $E_m$  at sub-daily fluctuations has a double crest centred at the same time-lag as for the  $A_m$  index. The lag-time correlation of *Dst* show a potential capability of prediction for equatorial disturbances with periods shorter than one day. The most important feature in Fig. 5 is the correlation with  $A_m$  and  $E_m$  between 1 to 10 days, suggesting a great capability for prediction, as seen by the lag-time peak correlations of  $\sim 0.65$  for high latitudes, and  $\sim 0.45$  for low latitudes. Values of time-delay at maxima correlation, and goodness of fit are given in Tab. 3. Dependencies on solar-cycle are similar for both high latitudes, so we modulate the northern parameterization (Eq. 4) for the fitting scheme of the southern parameterization (Eq. 5). The final output is the addition of both sub-daily and 1-10 day parameterizations. The resulting goodness of fits is provided in Tab. 3, and the parameterizations in supporting information.

285 Fig. 6 shows the resulting parameterization of  $A_m$  index to represent density disturbances ( $\rho < 10$  day) during 2006. The seasonal dependence (Fig. 4d) is clearly seen with lower density disturbances in the SPR ( $\rho_S$ ) around June. On the other hand, density disturbances at the equatorial Region ( $\rho_E$ ) and at the NPR ( $\rho_N$ ) maintain the magnitude of disturbances. Negative density enhancements precursors to geomagnetic storms are not well represented, probably due to a damping response associated with the nitric oxide cooling effects [Knipp et al., 2013]. Note that applying a 10-day running mean



290 filter, a false negative is introduced in both time-series of proxies and data. This is clearly shown in Fig. 6 with several negative values for the fit of  $Am$ . However, the residuals have bigger negative values than the  $Am$  parameterization (Fig. 6). This is due to negative values already present in the time-series (previous to apply the running-mean filter). Previous studies have shown that 37% of CME and 67% of CIR have an abnormal calm estate before geomagnetic storms [Denton et al., 2006; Borovsky and Steinberg 2006]. It has been suggested this effect might be triggered by the Russell-McPherron (R-M) effect, through a sector reversal just the upstream of the CIR stream interface.



295

**Figure 5.** Delay/correlation between residual density disturbances at 475 km altitude ( $\rho_r$ ) and the parameterizations of disturbances in terms of  $E_m$ ,  $Am$  and  $Dst$  indices, for (a) frequencies between 1 and 10 days and (b) sub-daily frequencies, for the northern ( $\rho_N$ ), equatorial ( $\rho_E$ ), and southern ( $\rho_S$ ) regions.



300

**Table 3. Best delay, correlation, and goodness of fit corresponding to Fig. 5.**

|                         |   | R-square | RMSE (kg/m <sup>3</sup> ) | Correlation | Delay (h) |       |
|-------------------------|---|----------|---------------------------|-------------|-----------|-------|
| 1 day < $\rho$ < 10 day | N | Dst      | 0.96                      | 1.5E-14     | 0.69      | -4.60 |
|                         |   | Am       | 0.96                      | 1.5E-14     | 0.64      | 4.60  |
|                         |   | Em       | 0.99                      | 7.6E-15     | 0.66      | 6.80  |
|                         | E | Dst      | 0.92                      | 1.7E-14     | 0.57      | -3.20 |
|                         |   | Am       | 0.98                      | 7.5E-15     | 0.47      | 5.60  |
|                         |   | Em       | 0.99                      | 6.9E-15     | 0.54      | 8.40  |
|                         | S | Dst      | 0.94                      | 2.1E-14     | 0.61      | -4.60 |
|                         |   | Am       | 0.93                      | 2.2E-14     | 0.63      | 4.60  |
|                         |   | Em       | 0.95                      | 2.0E-14     | 0.59      | 5.80  |
| $\rho$ < 1 day          | N | Dst      | 0.91                      | 1.5E-14     | 0.44      | -0.20 |
|                         |   | Am       | 0.92                      | 1.4E-14     | 0.44      | 2.80  |
|                         |   | Em       | 0.94                      | 1.2E-14     | 0.39      | 2.60  |
|                         | E | Dst      | 0.92                      | 1.1E-14     | 0.47      | 1.60  |
|                         |   | Am       | 0.99                      | 3.8E-15     | 0.47      | 4.40  |
|                         |   | Em       | 0.92                      | 1.2E-14     | 0.40      | 5.20  |
|                         | S | Dst      | 0.91                      | 2.2E-14     | 0.38      | -0.80 |
|                         |   | Am       | 0.94                      | 1.9E-14     | 0.46      | 2.20  |
|                         |   | Em       | 0.93                      | 1.9E-14     | 0.26      | 2.20  |



305

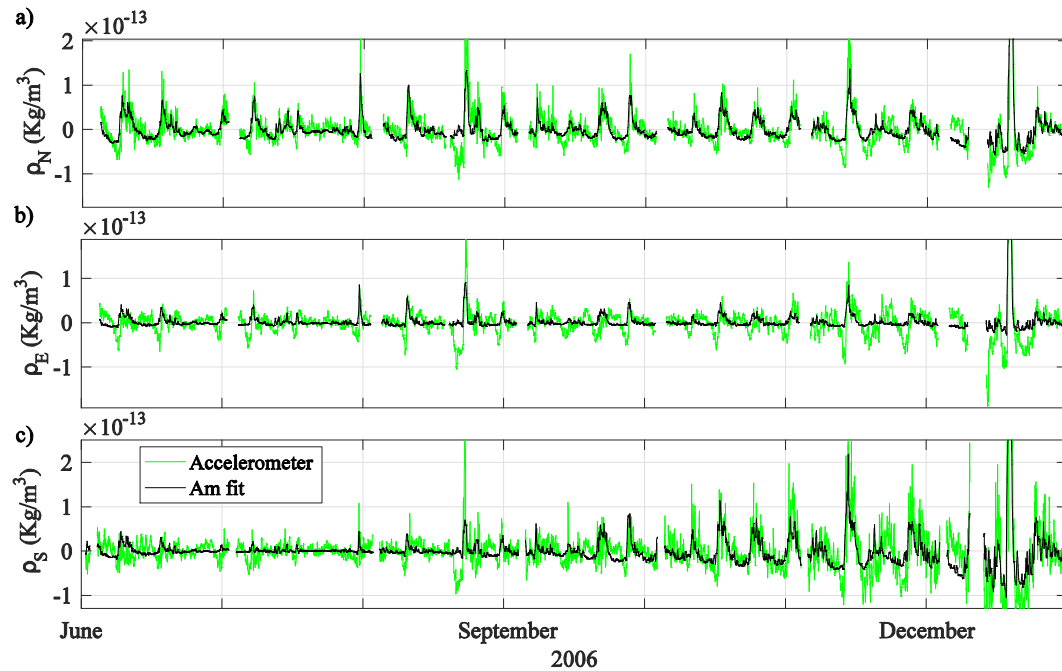
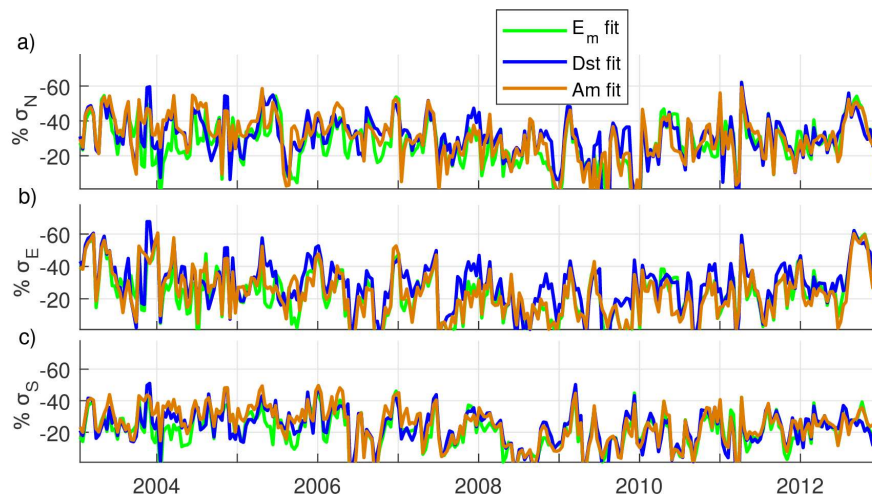


Figure 6. Thermospheric mass density disturbances ( $\rho < 10$  day) due to magnetospheric forcing at 475 km altitude during 2006, and the parameterization in terms of  $Am$  index, which is dependent on solar cycle and seasonal variation.



Comparing the results given in Tab. 3 with the previous studies, other authors are in good agreement with some particular differences, but no comprehensive analyses were presented concerning differences between SPR and NPR time-lag responses. For instance, *Bruinsma et al.* [2006] showed about 2 h time-delay at high latitudes with respect to solar wind indices and about 4 h for the equatorial regions, and *Rentz and Lühr* [2008] showed about 1 h time-lag with respect to  $E_m$ . For these authors, we obtain similar results for  $E_m$  at sub-daily fluctuations, but a difference of 2 h ahead for longer periods. *Zhou et al.* [2008] showed time lags of about 0-1 h and about 4 h to SYM-H and  $\Sigma Q$  indices, respectively, while our results for  $Dst$  are also null for sub-daily perturbations, and negative for longer periods (note that  $Dst$  and SYM-H are similar indices). *Muller et al.* [2009] showed about 3.5 h delay with respect to the  $Am$  index, and our time-lag for the same index is similar at sub-daily frequencies, but about 4-7 h for disturbances between 1-10 day period. *Guo et al.* [2010] showed density lag-times of about 3 h for high latitudes and about 4.5 h for low latitudes for IMF-derived indices, and *Liu et al.* [2010, 2011] showed a delay of about 4.5 h for the  $E_m$ . Our results show about 2 h longer (6-8 h at 1 to 10 days fluctuations). *Zhou et al.* [2013] showed delay times of about 1.5 h, 6 h, and 4.5 h at high, middle and low latitudes, respectively for  $E_m$ . *Iipponen and Laitinen* [2015] showed 7.5 h and 6 h for the Auroral Electrojet  $AE$  and the  $Ap$  indices, respectively, while our results fairly agree with our 6-7 h of time-lag provided by  $Am$  at 1 to 10 day disturbances. Since the wide range of delay-times provided in the literature does not differentiate the main signal from variations below 24 h, and none of the previous authors has investigated at least a complete solar cycle, we recommend the use of the values provided in Tab. 3.

We further investigate the change in the standard deviation of the residual density disturbances ( $\rho_r$ ) after the removal of parameterized disturbances, to provide an estimate about the uncertainty of the model, through multiplication of panels (a) to (c) in Fig. 7 with panels (b) to (d) in Fig. 2. In Fig. 7, the reduction in % of the standard deviation (30-day sliding window) is plotted for the northern, the equatorial, and the southern regions. Overall, the results show similar accuracy for all the period investigated, but with some hemispherical difference. The mean value of the reduction of standard deviation is about 30%, and peaks over the 50% are seen during all time-series, with slightly lower values at the SPR. The accuracy seems to decrease during low solar activity periods, most probably related to difficulties for fitting low values of disturbances. Taking Fig. 2 as reference, a reduction in 30% represents a reduction of standard deviation of about  $0.5 \cdot 10^{-13} \text{ kg/m}^3$  during high solar activity periods, and about  $0.06 \cdot 10^{-13} \text{ kg/m}^3$  during low solar activity periods, being both about the 5% of the background density. The parameterization using the  $Dst$  index show a larger reduction of residuals at the equator region and mostly during low solar activity, but a larger reduction at high latitude regions are given by the  $Am$  index under high solar activity conditions.  $E_m$  shows the lowest reduction levels during the declining of the solar cycle 23 (2003-2009), but seems to increase during the current solar cycle 24.

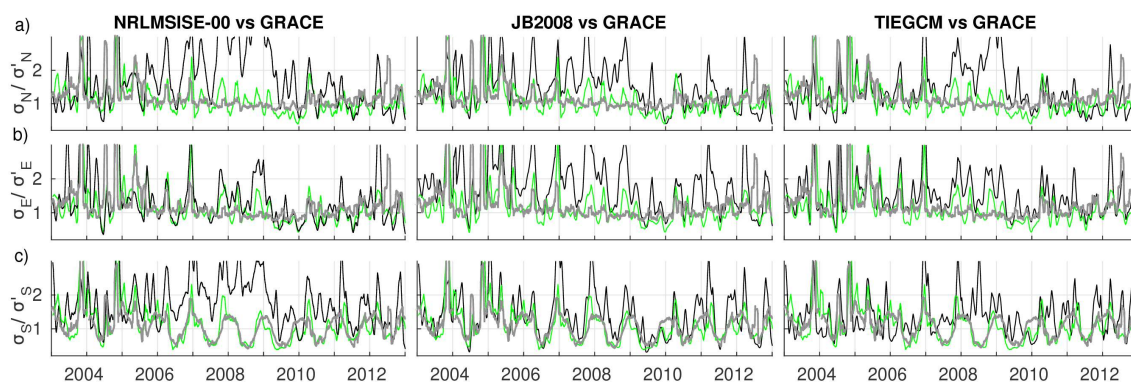


340 **Figure 7.** Reduction in % of the 30-day standard deviation sliding window of residual density disturbances at 475 km altitude ( $\rho_r$ ) when removing the parameterizations in terms of  $E_m$ , Am and Dst indices, and for (a) the northern, (b) the equatorial, and (c) the southern regions. Variations are below 10 day period.

Finally, we compare our results with three existing upper atmosphere empirical and physical (first-principles) models. We  
345 analyze a 10-year simulation of TIEGCM, NRLMSISE00, and JB2008 in the same way as the GRACE estimates. TIEGCM 2.0  
is computed at 5 min resolution using the 2005 Weimer model [Weimer, 2005] using IMF indices to drive high-latitude electric  
fields. Then, we estimate model densities at the same positions and times than the GRACE measurements along its orbital path.  
Finally, we employ solar-cycle, annual and LST dependencies modeled by the PCA of GRACE and the same filtering  
350 techniques detailed in the previous sections. Fig. 8 shows the same plots as Fig. 4 for GRACE results, but only for the variations  
between 1 and 10 day. The Fourier fits in terms of  $doy$  and  $E_m$  from Fig. 4, and the three models (TIEGCM, NRLMSISE00, and  
JB2008) are plotted along the GRACE results for comparisons. All three models overestimate the disturbance variability at the  
NPR during low solar activity (2007-2009). During high solar activity (2003-2006 and 2010-2013), the variations seem to fairly  
agree in all the cases. Variations at the equator are in better agreement with the models, while JB2008 slightly overestimates.  
These differences are most likely related to a miss-modeled dependence of the 11-year solar-cycle variability into the short-term  
355 disturbances of magnetospheric-forcing (refer to results shown in Fig. 2 and 3). This missing contribution shows an imbalance  
for the magnitude of disturbances between low and high solar-flux periods. Concerning the seasonal variation of magnitude of  
disturbances in the SPR, the semi-empirical model JB2008 shows best results, with best correlation to Fourier fits in terms of  
 $doy$  and  $E_m$ . The assimilation of accelerometer-based densities in the semi-empirical model JB2008 [Bowman *et al.*, 2008] might  
clearly contribute to better represent the actual thermospheric mass density disturbances due to magnetospheric forcing at the



360 SPR. On the other hand, during low solar activity, TIEGCM and NRLMSISE00 show bigger magnitude of disturbances during  
December in the opposite hemisphere (NPR). This feature is not shown from GRACE estimates and less pronounced for JB2008.



365 **Figure 8.** From top to bottom, the solar-flux normalized 30-day standard deviation sliding window of residual density disturbances  
at 475 km altitude ( $\rho_r$ ) at (a) the northern, (b) equatorial, and (c) southern regions, for NRLMSISE-00 (left), JB2008 (centred),  
and TIEGCM (right) models. Data of GRACE (green colour) and Furrier fits in terms of  $day$  and  $E_m$  (gray color) from Fig. 4 are  
included for comparison. Only variations between 1 and 10 day are represented.

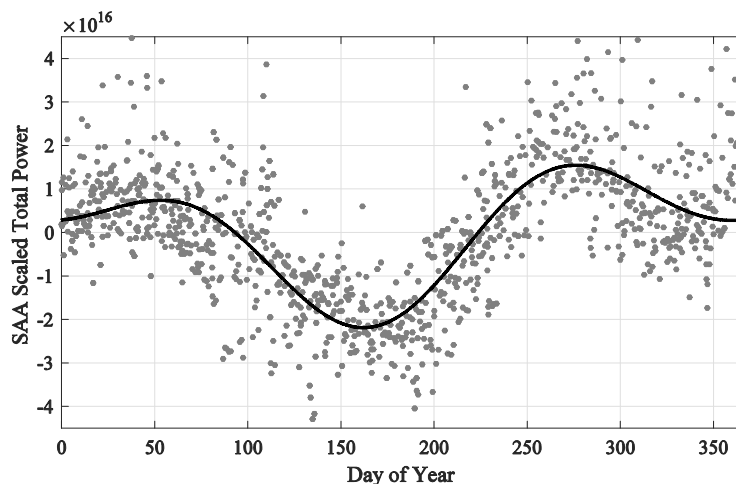
#### 4. Discussions

The hemispherical differential variability of thermospheric mass density disturbances due to the semi-annual variation of  
370 geomagnetic activity need to be discussed in relation to the lower disturbances seen during June solstice periods at the SPR  
(Fig. 4). The equinoctial-axial hypothesis of the semi-annual variation in geomagnetic activity was explained by the semi-  
annual variation of the effective southward component of the IMF in *Russell and McPherron* [1973]. The R-M effect holds  
that the southward IMF increases when the when the angle between the  $Z$  axis in geocentric solar magnetospheric (GSM)  
coordinate system and the  $Y$  axis in geocentric solar equatorial (GSEQ) coordinate system decreases. As mentioned above, a  
375 southward IMF will produce a more efficient reconnection and more energy can be introduced into the magnetosphere. This  
variability can be represented as two maximum around equinoxes, and a minimum around solstices [Zhao and Zong, 2012].  
We consider very probable this seasonal variation of magnetic range disturbance may transfer high quantities of energy in  
the MIT system. In fact, Schaefer et al. [2016] have shown a similar pattern on the intensity of the Southern Atlantic  
Anomaly (SAA). The SAA is a large region where the magnetic field is anomalously low and the radiation belt particles  
380 reach much lower altitudes than at similar latitudes around the globe. The authors showed that the intensity of the SAA-  
trapped proton (Van-Allen inner radiation belt) has a minimum around Solstice and maximum during equinox (Fig. 9). In  
this scheme, our assumptions might induce a tight coupling between the R-M variability and the energy transferred to the



MIT system, which is seen in these two cases as (1) an increase of energetic particles trapped in the radiation belts, and (2) an increase of energy transferred into the high latitude thermosphere. We therefore questioned if a similar pattern could be represented by our residuals in the equatorial and northern regions, and the resulting plot is shown in Fig. 10. In this plot, the residuals are presented to only show the seasonal variability, and a clear similitude to the R-M effect [Zhao and Zong, 2012] and to the pattern of the SAA intensity (Fig. 9) is shown with minimum values during solstices and maximum values around equinoxes. However, the pattern is more pronounced in the SPR, and a possible explanation can be given from the point of the irregular shape of the Earth's magnetic field.

As mentioned above, the SAA is formed because of the non-coincidence of the southern magnetic dip pole and the Earth's rotating axis. In a similar way, the anomalous low values of the magnetic field in the southern hemisphere during summer might facilitate the energy entrance in the thermosphere, creating relatively higher values during December than during June. In addition, previous studies have found that the extension of SAA decreases during geomagnetic storms, while high-energy protons precipitate from the cusps [Zou et al., 2015]. After a sharp decrease due to a geomagnetic storm, the SAA has shown to recover gradually over several months. Though, since it is questionable in which measure the contribution of the radiation belt can affect the variability of thermospheric mass density disturbances, we address this possible research for future work. In fact, high-energy particles in the Van Allen belts are only a minor source of energy flows into the thermosphere, while the dominant inflows arise from electric fields and auroral particles, such as those linked to the Dungey cycle.



400 Figure 9. The SAA intensity changes over the course of a year [Schaefer et al., 2016].

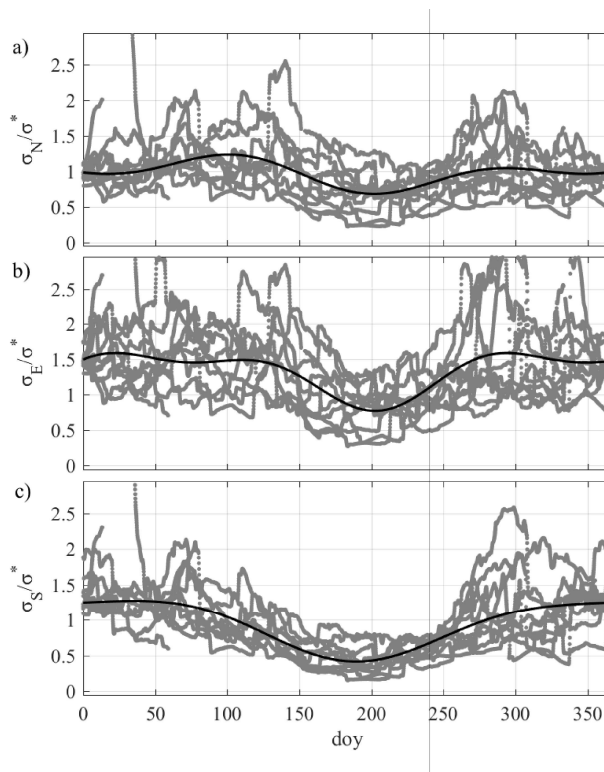


**Figure 10. Normalized residuals from this study showing only the seasonal variation (same as Fig. 4), for (a) the northern, (a) equatorial, and (c) southern regions. Fourier fit in black line.**

Then, under these assumptions and evidences, the equinox minimum disturbance in terms of the R-M effect offers a  
405 reasonable explanation for the seasonal variation in the magnitude of mass density disturbances due to magnetospheric  
forcing (Fig. 10). In addition, the irregular shape of the magnetic field, i.e., offset between the southern dip pole and the  
rotation axis, might enhance the effects in the SPR, creating the latitudinal asymmetric behaviour with enhanced  
disturbances during the summer of the southern hemisphere, effect which also is reflected by the SAA. We suspect these  
enhanced disturbances in the SPR during summer may be caused by an increased energy input through a weaker magnetic  
410 field in the noon sector. On the contrary in June solstice, since the northern Earth's magnetic dip pole is located near to the  
rotation axis ( $\sim 3^\circ$ ), the disturbances may be reduced due to a less compressed Earth's magnetic field. In fact, the evidence of  
the SAA is a clear example of the effects of the irregular shape of the magnetic field. These results and interpretations are  
consistent with the suggestions of an enhanced summer versus winter Joule heating at southern high latitudes of *Bruinsma et*  
*al.* [2006]; the very weak anomalies in the SPR during June solstice of *Rentz and Lüh* [2008]; and the 50 % greater  
415 dependence of mass density on *Dst* and *Ap* indices on the SPR than that in the NPR shown in *Ercha et al.* [2012].



These results support the potential improvement that can be gained from the use of parametric modelling of the density fluctuations with respect to magnetospheric proxies to improve predictions of thermospheric mass density perturbations, the resulting changes in satellite drag, and other derived physical parameters. Future studies resulting from the removal of mass density disturbances caused by the magnetospheric forcing can be addressed, but not restricted, to investigate additional  
420 turbulences, as for example, lower atmospheric waves including tides and planetary waves, recurrent TADs reaching the opposite pole and beyond, or the negative density enhancements during geomagnetic storms.

## 5. Summary and Conclusions

In this study, we have investigated the relationship between indices and mass density disturbances associated with magnetospheric forcing using 10 years (2003-2013) of GRACE observations, after accounting for annual, LST, and solar-  
425 cycle dependencies through the parameterization of the main PCAs. In the process, we have removed possible long-term trends in the data by focusing on disturbances on time scales smaller than 10-day period, and divided the analysis into sub-daily disturbances, and those between 1 and 10 days.

The results have shown unexpected fluctuation of disturbances due to solar-cycle variations, and an asymmetric fluctuation with lower values around June solstice at the SPR, hypothetically related to the R-M effect and the irregular shape of the  
430 Earth's magnetic field. We suspect that in the SPR during summer, when the R-M effect is minimum, density enhancements during storm-time periods may relatively be higher than during June, due to an increased energy input from a weaker side of the Earth's magnetic field, specifically that which originates the SAA. Notwithstanding, note that the amount of energy transferred from the Van Allen belts into the thermosphere is only a minor source of energy input, while processes linked to the Dungey cycle may dominate the main variability.

In this work, we have detected and parameterized annual and solar-cycle dependences included in thermospheric mass density disturbances due to magnetospheric forcing. We employ Pearson's linear correlation coefficients calculated with delay-times ranging from  $\pm 18$  h between estimates and parameterizations at three latitude regions to decipher the best fits. The parameterization in terms of *Dst* index has shown the best correlation, but without time-delay for prediction. The *Am* index and *E<sub>m</sub>* have shown the great potential as predictors. The *Am* and *E<sub>m</sub>* indices have provided similar correlation,  
440 residuals, and a time-delay of prediction at about 5-8 h. Employing the parameterizations here presented, the reduction of the standard deviation of mass density residual disturbances due to magnetospheric forcing at 475 km altitude reaches a mean value of 30%, and up to 60% of the total residual in several occasions, with respect to residuals from removing only solar-cycle, seasonal, and LST dependencies. The parameterizations provided in this manuscript can be re-scaled to required altitude and added to current models, where geomagnetic proxies should be set to *Am*=6 or equivalent.

Comparisons with JB2008, NRLMSISE-00, and TIEGCM models show their incapability to reproduce the seasonal and solar-cycle trends of disturbances. Similarities have been found at the equatorial region for the three models, but strong



discrepancies during low solar activity for NRLMSISE-00, and TIEGCM, showing a model overestimation of disturbance variability. While NRLMSISE-00 overestimates the disturbances during low solar activity at the SPR, JB2008 shows an impressive agreement with GRACE results, in terms of our hypothesis on the seasonal variation due to the R-M effect, and  
450 hemispheric asymmetry due to the irregular Earth's magnetic field.

This work represents a detailed statistical analysis important for future efforts to improve characterization, and, ultimately, prediction of the thermosphere. The main contributions in an easily understood manner are summarized as follows:

- An unexpected dependence on solar cycle, seasonal variation, and hemispheric asymmetry is found in the magnitude of high frequency ( $< 10$  day) thermospheric mass density disturbances due to magnetospheric forcing.
- 455 - The seasonal variation produces lower disturbances in June solstice, and the hypothesis of seasonal dependence on R-M effect is presented.
- The hemispheric asymmetry produces higher variability in the SPR, and we suspect a dependence on the irregular shape of the Earth's magnetic field.
- Correlation analysis is conducted using an extensive database (10 years) to provide time-lag values (below 1 h precision)  
460 for the currently employed magnetospheric proxies ( $A_m$ ,  $E_m$ , and  $Dst$ ) for thermospheric modelling.
- The high frequency disturbances ( $< 10$  day) have been parameterized in terms of the above dependencies and can be employed to improve current thermospheric models.

These new findings can substantially improve the understanding of the complex MIT system, and help to improve the modeling of thermospheric mass density variations, with the resulting changes in satellite drag.

#### 465 **Author contribution**

A Calabria designed and carried out the experiments, model, and manuscript. SG Jin provided mentorship and funding support.

#### **Acknowledgments**

This work is supported by the National Natural Science Foundation of China-German Science Foundation (NSFC-DFG)  
470 Project (Grant No. 41761134092), the Startup Foundation for Introducing Talent of NUIST (Grant No. 2243141801036), and the Talent Start-Up Funding project of NUIST (Grant No. 1131041901010). The authors declare that there is no conflict of interest regarding the publication of this paper. The GRACE data were obtained from the Information System and Data Center (ISDC) GeoForschungsZentrum (GFZ) website (<http://isdc.gfz-potsdam.de/>). Mass density estimates and models are provided in the supporting information files.



## 475 References

- Bates, D.R.: Some problems concerning the terrestrial atmosphere above 100 km level, *P. R. Soc. A.*, 253, 451–462, 1959.
- Bowman, B.R., Tobiska, W.K., Marcos, F.A., Huang, C.Y., Lin, C.S., and Burke, W.J.: A new empirical thermospheric density model JB2008 using new solar and geomagnetic indices, *AIAA/AAS Astrodynamic Specialist Conference*, AIAA 2008–6438, pp. 19, 2008.
- 480 Borovsky, J.E., and Steinberg, J.T.: The ‘‘calm before the storm’’ in CIR/magnetosphere interactions: Occurrence statistics, solar-wind statistics, and magnetospheric preconditioning, *J. Geophys. Res.*, 111, A07S10, 2006.
- Bruinsma, S., Forbes, J.M., Nerem, R.S., and Zhang, X.: Thermosphere density response to the 20–21 November 2003 solar and geomagnetic storm from CHAMP and GRACE accelerometer data, *J. Geophys. Res.*, 111, A06303, 2006.
- Bruinsma, S.L., and Forbes, J.M.: Large-scale traveling atmospheric disturbances (LSTADs) in the thermosphere inferred  
485 from CHAMP, GRACE, and SETA accelerometer data, *Journal of Atmospheric and Solar-Terrestrial Physics*, Volume 72, Issue 13, 2010.
- Calabia, A.: Thermospheric neutral density variations from LEO accelerometers and precise orbits, Ph.D. *Dissertation*, Chinese Academy of Sciences, China, 2017.
- Calabia, A., and Jin, S.G.: New modes and mechanisms of thermospheric mass density variations from GRACE  
490 accelerometers, *J. Geophys. Res. Space Physics*, 121(11), 11191–11212, 2016.
- Calabia, A., and Jin, S.G.: Thermospheric density estimation and responses to the March 2013 geomagnetic storm from GRACE GPS-determined precise orbits, *J. Atmos. Sol. Terr. Phys.*, 154:167–179, 2017.
- Deng, Y., and Sheng, C., Yue, X., Huang, Y., Wu, Q., Noto, J., Drob, D.P., and Kerr, R.B.: Interhemispheric asymmetry of ionospheric conductance and neutral dynamics, *AGU Fall Meeting Abstracts*, v.1, p.06, 2014.
- 495 Denton, M.H., Borovsky, J.E., Skoug, R.M., Thomsen, M.F., Lavraud, B., Henderson, M.G., McPherron, R.L., Zhang, J.C., and Liemohn, M.W.: Geomagnetic storms driven by ICME- and CIR-dominated solar wind, *J. Geophys. Res.*, 111, A07S07, 2006.
- Dungey, J.W.: Interplanetary magnetic fields and the auroral zones, *Phys. Rev. Lett.*, 6, 47–48, 1961.
- Ercha, A., Ridley, A.J., Zhang, D., and Xiao, Z.: Analyzing the hemispheric asymmetry in the thermospheric density  
500 response to geomagnetic storms, *J. Geophys. Res.*, 117, A08317, 2012.
- Forbes, J.M., Gonzalez, R., Marcos, F.A., Reville, D., and Parish, H.: Magnetic storm response of lower thermosphere density, *J. Geophys. Res.*, 101, 2313–2319, 1996.
- Fuller-Rowell, T.J.: The ‘‘thermospheric spoon’’: A mechanism for the semiannual density variation, *J. Geophys. Res.*, 103(A3), 3951–3956, 1998.
- 505 Fuller-Rowell, T.J., Codrescu, M.V., Rishbeth, H., Moffett, R.J., and Quegan, S.: On the seasonal response of the thermosphere and ionosphere to geomagnetic storms, *J. Geophys. Res.*, 101(A2), 2343–2353, 1996.



- Guo, J., Feng, X., Forbes, J.M., Lei, J., Zhang, J., and Tan, C.: On the relationship between thermosphere density and solar wind parameters during intense geomagnetic storms, *J. Geophys. Res.*, 115, A12335, 2010.
- 510 Iipponen, J., and Laitinen, T.: A method to predict thermospheric mass density response to geomagnetic disturbances using time-integrated auroral electrojet index, *J. Geophys. Res. Space Physics*, 120, 5746–5757, 2015.
- Kan, J.K., and Lee, L.C.: Energy coupling function and solar wind-magnetosphere dynamo, *Geophys. Res. Lett.*, 6, 577–580, 1979.
- Knipp, D., Kilcommons, L., Hunt, L., Mlynczak, M., Pilipenko, V., Bowman, B., Deng, Y., and Drake, K.: Thermospheric damping response to sheath-enhanced geospace storms, *Geophys. Res. Lett.*, 40, 1263–1267, 2013.
- 515 Lathuillère, C., Menvielle, M., Marchaudon, A., and Bruinsma, S.: A statistical study of the observed and modeled global thermosphere response to magnetic activity at middle and low latitudes, *J. Geophys. Res.*, 113, A07311, 2008.
- Lei, J., Thayer, J.P., Burns, A.G., Lu, G., and Deng, Y.: Wind and temperature effects on thermosphere mass density response to the November 2004 geomagnetic storm, *J. Geophys. Res.*, 115, A05303, 2010.
- Liu, H., Lühr, H., Henize, V., and Köhler, W.: Global distribution of the thermospheric total mass density derived from CHAMP, *J. Geophys. Res.*, 110, A04301, 2005.
- 520 Liu, H., and Lühr, H.: Strong disturbance of the upper thermospheric density due to magnetic storms: CHAMP observations, *J. Geophys. Res.*, 110, A09S29, 2005.
- Liu, R., Lühr, H., Doornbos, E., and Ma, S.-Y.: Thermospheric mass density variations during geomagnetic storms and a prediction model based on the merging electric field *Ann. Geophys.*, 28, 1633-1645, 2010.
- 525 Liu, R., Ma, S.-Y., and Lühr, H.: Predicting storm-time thermospheric mass density variations at CHAMP and GRACE altitudes, *Ann. Geophys.*, 29, 443-453, 2011.
- Liu, H., Thayer, J., Zhang, Y., and Lee, W.K.: The non-storm time corrugated upper thermosphere: What is beyond MSIS?, *Space Weather*, 15, 746–760, 2017.
- Lu, G., et al.: Interhemispheric asymmetry of the high-latitude ionospheric convection pattern, *J. Geophys. Res.*, 99(A4), 530 6491-6510, 1994.
- Marcos, F.A., Lai, S.T., Huang, C.Y., Lin, C.S., Retterer, J.M., Delay, S.H., and Sutton, E.K.: Towards next level satellite drag modeling, AIAA 2010-7840, paper presented at the AIAA Atmospheric and Space Environments Conference, Toronto, Ontario, Canada, 2–5 August, 2010.
- Müller, S., Lühr, H., and Rentz, S.: Solar and geomagnetic forcing of the low latitude thermospheric mass density as 535 observed by CHAMP, *Ann. Geophys.*, 27, 2087-2099, 2009.
- Picone, J.M., Hedin, A.E., Drob, D.P., and Aikin, A.C.: NRLMSISE-00 empirical model of the atmosphere: Statistical comparisons and scientific issues, *J. Geophys. Res.*, 107(A12), 1468, 2002.
- Qian, L., Burns, A.G., Emery, B.A., Foster, B., Lu, G., Maute, A., Richmond, A.D., Roble, R.G., Solomon, S.C., and Wang, W.: The NCAR TIE-GCM, in *Modeling the Ionosphere-Thermosphere System* (eds J. Huba, R. Schunk and G. Khazanov), 540 John Wiley & Sons, Ltd, Chichester, UK, 2014.



- Rentz, S., and Lühr, H.: Climatology of the cusp-related thermospheric mass density anomaly, as derived from CHAMP observations, *Ann. Geophys.*, 26, 2807–2823, 2008.
- Schaefer, R.K., Paxton, L.J., Selby, C., Ogorzalek, B.S., Romeo, G., Wolven, B.C., and Hsieh, S.-Y.: Observation and modeling of the South Atlantic Anomaly in low Earth orbit using photometric instrument data, *Space Weather*, 14, 330–342, 545 2016.
- Sutton, E.K., Forbes, J.M., and Nerem, R.S.: Global thermospheric neutral density and wind response to the severe 2003 geomagnetic storms from CHAMP accelerometer data, *J. Geophys. Res.*, 110, A09S40, 2005.
- Sutton, E.K., Forbes, J.M., and Knipp, D.J.: Rapid response of the thermosphere to variations in Joule heating, *J. Geophys. Res.*, 114, A04319, 2009.
- 550 Tapley, B.D., Bettadpur, S., Watkins, M., and Reigber, C.: The gravity recovery and climate experiment: Mission overview and early results, *Geophys. Res. Lett.*, 31, L09607, 2004.
- Weimer, D.R.: Improved ionospheric electrodynamic models and application to calculating joule heating rates, *J. Geophys. Res.* 110, 2005.
- Zhao, H., and Zong, Q.-G.: Seasonal and diurnal variation of geomagnetic activity: Russell-McPherron effect during 555 different IMF polarity and/or extreme solar wind conditions, *J. Geophys. Res.*, 117, A11222, 2012.
- Zhou, Y.L., Ma, S.Y., Lühr, H., Xiong, C., and Reigber, C.: An empirical relation to correct storm-time thermospheric mass density modeled by NRLMSISE-00 with CHAMP satellite air drag data, *Adv. Space Res.*, 43, 819–828, 2008.
- Zhou, Y.L., Ma, S.Y., Liu, R.S., Luehr, H., and Doornbos, E.: Controlling of merging electric field and IMF magnitude on storm-time changes in thermospheric mass density, *Ann. Geophys.*, 31, 15-30, doi:10.5194/angeo-31-15-2013, 2013.
- 560 Zou, H., Li, C., Zong, Q., Parks, G.K., Pu, Z., Chen, H., Xie, L., and Zhang, X.: Short-term variations of the inner radiation belt in the South Atlantic anomaly, *J. Geophys. Res. Space Physics*, 120, 4475–4486, 2015.